Astronomy & Astrophysics manuscript no. ms
May 5, 2026
©ESO 2026

Signatures of coronal mass ejections in differential emission measure analysis of the Sun as a star

Angelos Michailidis[1,2,3] and Spiros Patsourakos[3]

[1] Department of Physics, National and Kapodistrian University of Athens, University Campus, Zografos, GR-157 84 Athens, Greece
[2] Research Center for Astronomy and Applied Mathematics, Academy of Athens, Soranou Efesiou Str., 4, 11527, Athens, Greece
[3] Physics Department, University of Ioannina, Ioannina GR-45110, Greece
e-mail: a.michailidis@uoi.gr

Received ; accepted

arXiv:2603.24791v2 [astro-ph.SR] 4 May 2026

ABSTRACT

Aims. For this work we investigated whether signatures of coronal mass ejections (CMEs) can be retrieved in the differential emission measure (DEM) resulting from extreme-ultraviolet (EUV) observations of the Sun as a star.
Methods. We analyzed a set of 16 major (above the M1.0 class of the Geostationary Operational Environmental Satellites classification), eruptive (i.e., associated with CMEs) flares. For each flare we constructed light curves of the average intensity of full-disk images taken by the Atmospheric Imaging Assembly (AIA) on board the Solar Dynamics Observatory (SDO) mission in EUV channels centered at 94, 131, 171, 193, 211, and 335 Å . The light curves comprise both the pre-flare and post-flare phases of the associated flares. We also corrected the light curves for the gradual phase of the associated flare.
Results. From the analysis of the full-disk light curves we find that all the studied flares exhibit dimmings, where the intensity decreases with respect to the pre-flare phase, mainly in the 171, 193, and 211 Å channels. The dimmings in these channels become more pronounced upon applying the gradual-phase correction. Calculation of the DEM from the intensities of the six employed AIA EUV channels shows that during all the observed dimmings, the DEM decreases with respect to its value in the pre-flare phase in the temperature range $\approx 10^{5.7} - 10^{6.3}$ K. The signature of the dimming is more pronounced in the temperature range of $\approx 10^{5.7} - 10^{6.0}$ K for the DEMs calculated with the original light curves, and in the range of $\approx 10^{6.0} - 10^{6.3}$ K for the DEMs that were calculated by taking into account the gradual-phase correction. For a sample event of our database, we also calculated DEMs from EVE and spatially resolved AIA observations of the source region of the corresponding dimming in order to assess the impact of spectral resolution and full-disk averaging. For both these cases the temperature range where the dimming in the DEM is more pronounced is similar to that resulting from the analysis of the spatially averaged AIA data; the magnitude of the dimming in the DEM is similar for the EVE and larger for the spatially resolved AIA observations compared to the Sun-as-a-star AIA observations, respectively.
Conclusions. Coronal dimmings associated with CMEs can be detected in Sun-as-a-star DEMs derived from EUV observations. The gradual phase of the associated flare can lead to an underestimation of the magnitude of the dimming in the intensities and in the DEMs. The application of the correction alters the temperature range in which the signature of the dimming in the respective DEMs is more pronounced.

Key words. Sun: activity – Sun: corona - Sun: coronal mass ejections (CMEs) - Sun: flares - Sun: transition region - Sun: UV radiation

1. Introduction

Coronal mass ejections (CMEs) are large-scale expulsions of magnetized plasmas from the solar corona into the interplanetary space. They are most commonly observed with coronagraphs, which block the intense radiation of the solar disk and reveal the much fainter structures of the corona. Their initial stages are tracked by mainly extreme-ultraviolet (EUV) and soft X-ray (SXR) telescopes observing the solar disk and the low corona. Studying, understanding, and forecasting CMEs is not only an important astrophysics problem, but is also crucial for the smooth operation of space systems, as CMEs represent a major driver of the most extreme space-weather manifestations via their intense magnetic fields, enhanced momentum budgets, and their accelerated particles (for detailed reviews on CMEs and their space weather implications, see, e.g., Chen 2011; Webb & Howard 2012; Vourlidas et al. 2019; Temmer 2021; Zhang et al. 2021).

Multiwavelength high spatio-temporal resolution EUV and SXR observations of CME onsets in the low corona reveal their multifaceted manifestations and aspects in terms of various interrelated phenomena and morpological features, including expanding loops, cavities, flux ropes, EUV waves and shocks, and dimmings (e.g., check the review Webb & Howard 2012). Dimmings are transient decreases in the EUV and SXR intensities at and around the source regions of CMEs; they frequently occur in tandem with flares in the low corona, are frequently observed, and are interpreted as an effect of the mass evacuation due to the ongoing CMEs (e.g., Hudson et al. 1996; Reinard & Biesecker 2008; Harra & Sterling 2001; Patsourakos et al. 2010; Mason et al. 2014; Dissauer et al. 2018; Jin et al. 2022) (for a recent review on solar and stellar dimmings, see Veronig et al. 2025). The characteristics of EUV dimmings depend on (among other things) the mass of the CME (Aschwanden et al. (2009)). Three-dimensional modeling of the EUV dimming can provide information about the direction of the CME during the early stages of its evolution (Jain et al. (2024)). Not all CMEs have associ-

ated EUV dimmings. As shown in Robbrecht et al. (2009), there can be CMEs with no low-corona signatures in the EUV. These events occur in the quiet Sun, where the magnetic field is weak, and mainly during solar minimum periods.

Coronal mass ejections are not only important for terrestrial space weather, but for exoplanetary space weather as well. Stellar CMEs may strip an exoplanet's atmosphere; the most vulnerable ones are those orbiting around magnetically active dwarf stars. Therefore, stellar CMEs may play a significant role in the habitability of exoplanets. This topic is discussed in detail in Lammer et al. (2007), Airapetian et al. (2020), and Samara et al. (2021). Given that stars other than the Sun are mostly observed as point sources, Sun-as-a-star studies, i.e., collapsing the Sun into a point source, offer important clues to pertinent studies of other mainly Sun-like stars (e.g., Mason et al. 2016; Veronig et al. 2021; Xu et al. 2022). For example, as we cannot directly image stellar CMEs, stellar dimmings could be used as a "smoking gun" of ongoing stellar CMEs. Mason et al. (2025) showed that CME-induced stellar dimmings can be detectable in the EUV.

Several recent studies followed this path, and studied the Sun as a star and stellar dimmings. Mason et al. (2016) investigated Sun-as-a-star observations for a set of 37 dimming events, some of them associated with eruptive flares spanning B9.0-X6.9 of the Geostationary Operational Environment Satellites (GOES) classification using irradiances recorded by the Extreme Ultraviolet Variability Experiment (EVE) instrument (Woods et al. (2012)) on board the Solar Dynamics Observatory (SDO). EVE observes the EUV solar irradiance, i.e., disk-integrated intensity, from 10 to 1050 Å with a spectral resolution of 1 Å and a temporal resolution of a few seconds. For a subset of 17 of the dimming events for which they were able to infer both dimming and associated CME parameters, they found a strong positive correlation (Pearson correlation coefficient 0.75) between the CME mass and the square root of the dimming depth (i.e., the percentage-wise decrease in the intensity during dimmings with respect to its pre-flare value). This empirical result could be used as a tool to infer the mass of ongoing CMEs from the associated EUV dimmings.

Veronig et al. (2021) generated broadband Sun-as-a-star light curves at a 10 s cadence by integrating time series of EVE spectra in the wavelength range 15–25 nm for a set of 38 major flares (GOES class M5 and above). Thirty-two of the analyzed CMEs showed dimmings and only 1 of the 33 detected dimmings was not associated with a CME, thus suggesting a tight mutual association between CMEs and dimmings. The dimmings retrieved in EUV irradiance by EVE were also consistent with spatially resolved EUV dimmings, i.e., derived by integrating the AIA intensities in boxes encapsulating the source regions of the associated CMEs. Median dimming depths of 2.18 (22.7) % for solar (stellar) dimmings were found. Moreover, Veronig et al. (2021) used the Atmospheric Imaging Assembly (AIA) (Lemen et al. 2012) on board SDO to find full-Sun light curves in the 193 Å, and found that 39 of the 53 eruptive flares exhibited dimmings. Xu et al. (2024) studied several eruptive filaments using AIA and EVE, and found dimmings in EVE with depths ranging from 1% to 6.2%. These dimmings last from 0.4 hours to 7 hours. Additionally, they found a positive corelation between dimming depth and filament area. This result may be used as a diagnostic tool for the size of stellar filaments.

From the discussion above it appears that the bulk of Sun-as-a-star observations of EUV dimmings have focused on the analysis of intensities. The differential emission measure (DEM) is an important tool in the study of the atmospheres of the Sun and other stars, and is used to characterize the thermal structure of optically thin plasmas, such as the solar corona (e.g., the review of Del Zanna & Mason 2018). It quantifies the distribution of plasma as a function of its temperature T; it can be written as $DEM(T) = n^2 dh/dT$, where n is the electron density and dh the infinitesimal length along the line of sight. To determine $DEM(T)$, inversions are applied to the intensities either derived from observations or synthesized from models. The intensities, usually recorded in the EUV and SXR domains, refer to spectral lines, narrowband channels centered at some strong line, or broadband channels. Loyd et al. (2022) used far-ultraviolet observations of dimmings associated with flares in ϵ Eridani, and discuss their relevance with respect to stellar CMEs. They also present the emission measure distribution of ϵ Eridani, which exhibits a peak in the temperature range of $10^{6.4}$ to $10^{6.8}$ K.

Therefore, the goal of our study is to investigate whether EUV dimmings associated with CMEs can have a signature in DEMs resulting from Sun-as-a-star EUV observations. A data source to perform this task could be EVE owing mainly to its relatively high spectral resolution in the EUV, i.e., 1 Å. We opted to employ AIA Sun-as-a-star observations for the following reasons. First, and most importantly, results from AIA Sun-as-a-star observations can be directly compared with the spatially resolved AIA observations of the related dimming source region(s) of the analyzed event(s). This could allow us to directly assess the impact of using full-disk averages on the associated DEMs. Additionally, spatially resolved AIA observations of dimmings allow us to infer the contribution of the source ARs of the associated CMEs to the dimmings obtained in Sun-as-a-star observations. Second, AIA employs narrowband EUV observations over bandpasses spanning a few angstroms, which gives rise to higher signal-to-noise ratios compared to instruments with narrower bandpasses (e.g., EVE). We finally note that many studies used spatially resolved AIA observations to calculate DEMs. To this end, we used the spatially averaged intensities from full-disk EUV images at 12 s cadence taken by AIA during 16 major eruptive flares showing evidence of dimmings to calculate the associated light curves, and then calculated the respective DEMs. For all our analyzed events we calculated the fraction of pixels undergoing dimming within and around each respective CME source region to that of pixels undergoing dimming in full-disk AIA images, which allowed us to assess the contribution of the source AR dimmings to the dimmings observed across the entire solar disk. Finally, and as a further benchmarking of various data sources, we compared the DEM from our Sun-as-a-star AIA observations for a sample event with those resulting from EVE and spatially resolved AIA observations of the source region of the analyzed event. This allowed us to assess the impact of spectral resolution and full-disk integration on the resulting DEMs, respectively. Section 2 discusses our dataset, the respective methodology and its application to our data and Section 3 contains an overview of our results and a short discussion.

2. Data analysis

For this work we analyzed Sun-as-a-star EUV observations of eruptive flares performed with AIA. AIA takes 4096 × 4096 pixel images of the solar disk and lower corona, with a field of view extending to about 0.5 R_s above the solar limb at a 12 s cadence. We analyzed a set of 16 major eruptive flares above M1.0 of the GOES classification. Table 1 contains several elements of the analyzed events. These events were extracted from the tables of Veronig et al. (2021) and Hernandez Camero et al.

(2025). The starting and peak times, the GOES classification, and the source active regions and their coordinates of the analyzed eruptive flares were retrieved from Solar Monitor (Gallagher et al. 2002). The GOES classification is also listed in the Veronig et al. (2021) and Hernandez Camero et al. (2025) tables. For the classification of the associated CMEs as halo or non-halo, we used the CDAW LASCO CME catalog (Yashiro et al. 2004). The CME–flare association was established based on the temporal correspondence between the event times listed in the Veronig et al. (2021) and Hernandez Camero et al. (2025) tables and the recorded SXR peak time (see Table 1), allowing for a temporal offset of a few minutes between the two. To investigate whether an eruptive filament was observed during the analyzed events we consulted the list of McCauley et al. (2015); the respective results can be found in the 10th column of Table 1. Only 5 out of the total 16 analyzed events were associated with filament eruptions, either full or partial.

To investigate the connection between the source ARs of the analyzed events with spatially resolved observations of dimmings, we consulted 2D maps of detected dimmings from the Solar Demon Dimming Detection database of the Solar Influences Data Analysis Center (SIDC).[1] In the left panel of Fig. 1, and using a 171 Å image, we show the source AR of the fifth event of Table 1 enclosed in the red box; the right panel of this figure supplies a 2D map of the dimmings detected by Solar Demon on a almost cotemporal AIA 211 Å image. The choice of the red box certainly involves some degree of subjectivity, but its choice is made so as to include both the source AR and its surroundings, given that CME-related dimmings also span over locations around their source regions (e.g., Veronig et al. 2025). The source AR is located roughly at the center of the box, although we allowed some freedom in order to include dimmings that are not symmetrically distributed around the AR. It seems as if a significant fraction of the pixels with dimming, shown in white in the right panel of Fig. 1, are concentrated on or around the source AR, which suggests that the main contributor to Sun-as-a-star observations of the associated dimming arises from the source AR of the respective eruptive flares. We reached essentially the same conclusion from inspection of analogous plots for the remaining events of Table 1, which are available in our online Zenodo database.[2]

In the 11th column of Table 1 we present the percentages of the pixels undergoing dimming (white pixels in the right panels of the respective online images) that are inside the red boxes over the total number of pixels undergoing dimming for each event of Table 1. The red boxes, on and around the source ARs, contain significant fractions (≈22.0 to 91.5 %) of the pixels undergoing dimmings in the full-disk AIA images. For events 10, 13, 14, and 16 in Table 1, we note that the dimmings are significantly scattered on the solar disk, thus leading to the smaller percentages of pixels undergoing dimming in the range of ≈22.0 - 40.0%.

2.1. Construction of Sun-as-a-star light curves

To build light curves of the Sun as a star in the EUV for our events, and given that AIA takes spatially resolved images of the solar disk and the low corona, we used the average intensity per considered image. This essentially degrades the Sun into a point source, i.e., a single pixel, as appropriate for observations of stellar flares. For each event, we considered 12 s cadence level

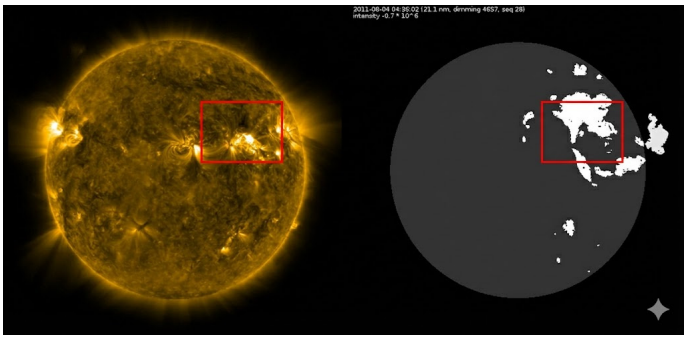

Fig. 1: Left: Source AR of the eruptive flare of the fifth event in Table 1 (red box) in a 171 Å image. Right panel: Detected dimmings from the Solar Demon database (in white) in an almost cotemporal 211 Å channel image.

1 AIA images in its six EUV channels, centered at 94, 131, 171, 193, 211, and 335 Å for intervals spanning from about 2 hours before the peak time of the associated SXR flare up to 6 hours past this time. This means that for each event we considered approximately 14,400 images. To mitigate the overhead from using large stocks of data, we only downloaded the headers of the images. The average intensity for each image we used in the construction of the light curves corresponds to the DATAMEAN keyword value of the respective Flexible Image Transfer System (fits) file header; to obtain average intensities in units of data number per second (DN/s), we divided the DATAMEAN keyword value with the corresponding exposure time in s, stored in the EXPTIME keyword. We therefore used these spatially averaged and exposure-normalized intensities in the construction of the light curves that we used in our analysis. We note here that by downloading a limited set of images, and by calculating the corresponding averaged intensities, we confirmed consistency with the DATAMEAN keyword value of the associated fits files headers. Finally, to ensure that our analysis of dimmings is accurate, we made sure that the light curves of the selected events did not feature any trends (either upward or downward) in the pre-flare time interval.

2.2. Correction of gradual-phase of the Sun-as-a-star light curves

Given that our light curves comprise contributions from the entire Sun, it is therefore possible that Sun-as-a-star AIA dimmings could be affected by the EUV gradual phase of flares discussed in the frame of EVE irradiance observations in Mason et al. (2014, 2016). In essence, plasma cooling after the SXR peak of the associated flare, could give rise to emission peaks and enhancements that are cotemporal with the ongoing dimmings. This in turn, may lead to an underestimation of the dimming magnitude. Therefore, a correction for this is warranted in order to obtain better estimates of the studied dimming properties. Mason et al. (2014) proposed a gradual-phase correction of EVE observations, based on the use of dimming and non-dimming spectral lines, i.e., respectively showing and not showing evidence of dimming in the light curves.

We adapted the (Mason et al. 2014) gradual-phase correction method for the case of our AIA observations. The 171, 193, and 211 Å channels were treated as dimming channels; therefore, we implemented our gradual-phase correction only for these channels. For all analyzed events, the 335 Å non-dimming channel

[1] https://www.sidc.be/solardemon/science/dimmings.php?did=4694&science=1
[2] https://zenodo.org/records/18412555

Table 1: Eruptive flares and associated CMEs in our study.

Index	SXR Start (UT)	SXR Peak (UT)	GOES Class	AR NOAA Number	Halo CME	Coordinates (arcsec)	Correction	Database	Eruptive Filament	Percentage (%)
1	2010-08-07 17:55:00	2010-08-07 18:24:00	M1.0	11093	Yes	(-500,200)	Yes	2	No	91.50
2	2011-02-15 01:44:00	2011-02-15 01:56:00	X2.2	11158	Yes	(250,-200)	Yes	1	Yes	83.82
3	2011-06-07 06:16:00	2011-06-07 06:41:00	M2.5	11226	Yes	(700,-350)	Yes	2	Partial	86.06
4	2011-08-03 13:17:00	2011-08-03 13:48:00	M6.0	11261	Yes	(500,200)	Yes	1	No	86.05
5	2011-08-04 03:41:00	2011-08-04 03:57:00	M9.3	11261	Yes	(650,200)	Yes	1	Yes	47.55
6	2011-08-09 07:48:00	2011-08-09 08:05:00	X6.9	11263	Partial	(800,250)	Yes	1	No	66.68
7	2011-09-06 01:35:00	2011-09-06 01:50:00	M5.3	11283	Yes	(200,150)	Yes	1	No	87.51
8	2011-09-06 22:12:00	2011-09-06 22:20:00	X2.1	11283	Yes	(200,150)	Yes	1	No	89.34
9	2012-01-23 03:38:00	2012-01-23 03:59:00	M8.7	11402	Yes	(450,550)	Yes	1	Partial	66.14
10	2012-03-07 00:02:00	2012-03-07 00:24:00	X5.4	11429	Yes	(-300,400)	Yes	1	No	30.41
11	2012-07-06 23:01:00	2012-07-06 23:08:00	X1.1	11515	Yes	(550,-300)	Yes	1	No	83.44
12	2013-11-10 05:08:00	2013-11-10 05:14:00	X1.1	11890	Partial	(350,-200)	Yes	1	No	85.17
13	2013-11-19 10:14:00	2013-11-19 10:26:00	X1.0	11893	No	(950,-200)	Yes	1	No	39.31
14	2014-01-07 18:04:00	2014-01-07 18:32:00	X1.2	11944	Yes	(0,-100)	Yes	1	No	36.99
15	2014-02-25 00:39:00	2014-02-25 00:49:00	X4.9	11990	Yes	(-850,-100)	Yes	1	Yes	66.91
16	2014-04-18 12:31:00	2014-04-18 13:03:00	M7.3	12036	Yes	(550,-100)	Yes	1	No	22.45

Notes. First column: Event index; second and third columns: Start and peak time of the GOES flare; fourth column: GOES flare class; fifth column: National Oceanic and Atmospheric Administration (NOAA) source active region (AR); sixth column: Associated CME halo descriptor; seventh column: Heliocentric coordinates of the source AR of the CMEs; eighth column: Use of gradual phase correction of dimming channels in *DEM* calculations; ninth column: Database from which the event was obtained (1 for Veronig et al. (2021) and 2 for Hernandez Camero et al. (2025)); tenth column: Eruptive filament associated with the analyzed eruptive flare (McCauley et al. 2015); eleventh column: Percentage of pixels undergoing dimming inside the red box in the Zenodo database.[a]

[a] `https://zenodo.org/records/18412555`.

was used in the gradual-phase correction. The only exception is the 2014 April 18 event (index 16 in Table 1), for which we used the 94 Å channel instead of 335 Å because in this particular event a dimming was also observed in the 335 Å channel. We did not, however, correct the 335 Å channel intensities, in order to be consistent in the analysis of all events.

Our gradual-phase correction method involves the following steps:

1. applying a Gaussian smoothing window with $\sigma = 5$ (i.e., 1 minute) to the original Sun-as-a-star light curves of all six AIA EUV channels, resulting in smoother light curves $I_s(t)$;
2. calculating the fractional (i.e., dimensionless) variation of each light curve with respect to its pre-event value, $\frac{I_s(t)-I_{start}}{I_{start}}$, with I_{start} corresponding to the mean value of the first 200 images of the respective $I_s(t)$;
3. aligning the flare peaks of the dimming and non-dimming channel light curves;
4. scaling down the light curve with the larger peak value so that the two peaks are equal;
5. cropping the edges of the aligned light curves to ensure they are of the same length;
6. subtracting the temporally aligned non-dimming light curve from the dimming light curve. This yields a dimensionless corrected light curve $I'_{corr}(t)$;
7. converting back to DN/s units by applying the formula $I_{corr}(t) = (I'_{corr}(t) + 1) \times I_{start}$, where $I_{corr}(t)$ is the corrected light curve in DN/s units. Essentially, this formula returns the $I_s(t)$ value plus a value corresponding to the correction. This conversion is warranted, given that the calculation of DEMs (see next section) requires intensities in DN/s units.

It should be noted that unlike (Mason et al. 2014), who used spectrally resolved EVE data with many different dimming and non-dimming spectral lines to perform the gradual-phase correction, in our analysis we were limited by the small number of available AIA EUV channels (six). Nevertheless, the resulting corrections seemed reasonable, given that they maintained the shape of the original light curves, and we therefore also used the corrected light curves for further analysis. In the following, and for brevity, we use the term correction in place of gradual-phase correction.

In Fig. 2 we show an example event corresponding to the fifth event listed in Table 1. The original light curves are in blue and their smoothed versions in orange. The corrected light curves (featured in the 171, 193, 211 Å dimming channels) are plotted in red. The red-shaded box corresponds to a pre-event temporal window, the green-shaded box encloses a temporal window around the maximum dimming for the original (i.e., not corrected) light curves, and the blue-shaded window encloses a temporal window around the maximum dimming for the corrected light curves. In the remainder of the paper we denote by pre-event, uncorrected dimming, and corrected dimming windows the temporal windows respectively corresponding to those defined above. Each window corresponds to 200 images (40 minutes). In our follow-up analysis we calculated the average intensity for each window as a proxy of the pre-event and dimming stages of the analyzed events. Using such windows was beneficial for several reasons. First, by averaging the intensities within each window we increased the signal-to-noise ratio of the resulting average intensities. Second, by considering an average intensity over the pre-event window we obtain a more representative picture, devoid of the impact of small-scale fluctuations. Third, using the extended dimming windows allows for possible small temporal offsets between the dimmings in various AIA channels.

In Fig. 2 we see that the dimming appears in the 171, 193, and 211 Å channels, and the corrected curves show a deeper dimming than the uncorrected curves, as expected. These three channels have peak-response temperatures of about $10^{5.7}$ K to $10^{6.3}$ K. We also see that in the corrected curves, the maximum value of dimming appears earlier than in the uncorrected curves.

In general, the dimming is observed for almost all events in these three channels (171, 193, 211 Å). The only exceptions are the events with Table 1 indices 2, 9,16. In event 2, the dimming is observed only in the 171 Å for the uncorrected light curves, but in all three dimming channels for the corrected light curves. In event 9 there is no dimming for the 211 Å channel for the uncorrected light curve, but there is for the corrected light curve. Finally, in event 16 there is also a modest dimming in the 335 Å channel, which is the reason why, for this particular event we applied the correction using the 94 Å channel, as described above.

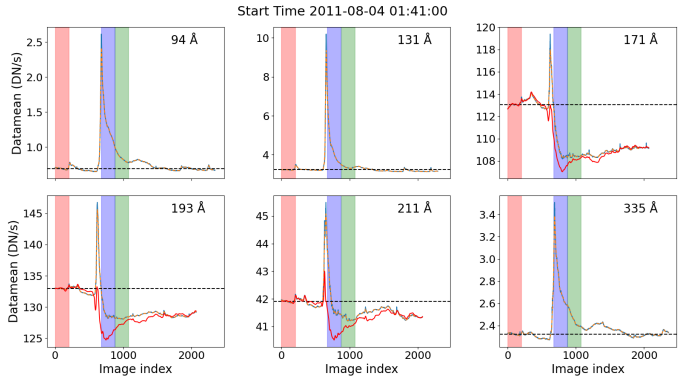

Fig. 2: Sun-as-a-star light curves for the 94, 131, 171, 193, 211, and 335 Å channels of AIA for event 5 in Table 1). The blue lines are the original light curves, the dashed orange lines are smoothed, and the red lines are corrected. The red-, green-, and blue-shaded vertical boxes correspond to the pre-event, dimming window (for the original light curves), and dimming window (for the corrected light curves), respectively. For this event the correction worked as intended.

As a further test for our correction, we used the Solar Demon Dimming Detection database of the Solar Influences Data Analysis Center (SIDC) (Kraaikamp, Emil & Verbeeck, Cis 2015). The SIDC database has light curves of areas on the solar disk experiencing dimmings in the 211 Å channel. All of the events included in our analysis are also included in the SIDC database. We confirmed that the shape of our corrected light curves for the 211 Å channel match relatively well the shape and the timing of the respective SIDC light curves, thus supplying extra credibility to our correction.

As a visualized summary of our results for all the analyzed events, in Fig. 3 we show boxplots of the ratio, $d_{dimming}$, of the average intensity of the pre-event window to that corresponding to the dimming window for the three dimming channels (171, 193, 211 Å).

The box extends from the first quartile (25 %) to the third quartile (75 %) of the data, with a horizontal line denoting the median (50%) values of the $d_{dimming}$ distributions. The whiskers span 1.5 times the inter-quartile (IQR) range. In Fig. 3 we present boxplots for both the uncorrected and the corrected light curves, left and right panel, respectively. In the left panel $d_{dimming}$ is calculated using the original (uncorrected) light curves. In the right panel we used the corrected light curves in the calculation of $d_{dimming}$.

In both cases (left and right panel) we see dimming in the three included channels. For the left panel, the median value of $d_{dimming}$ is approximately 0.96, 0.97, and 0.99 for the 171, 193, and 211 Å channels, respectively. For the right panel, the respective median values of $d_{dimming}$ are approximately 0.96 (slightly less than the left panel), 0.95, and 0.97. Therefore, the application of the correction leads to smaller $d_{dimming}$ median values, especially for the 193 and 211 Å channels. The median values are situated more or less in the middle of the respective boxes, with the exception of the corrected 171 Å channel case. This implies symmetric $d_{dimming}$ distributions. In addition, the upper error bars of the boxplots for the corrected light curves, are below one. Regarding the size of the boxes and the whiskers, in all of the 171 and 193 Å channels, the boxes in the left panel are larger than the respective ones in the right panel, while the opposite is true for the 193 Å channel. This suggests that the correction of the gradual-phase leads to narrower $d_{dimming}$ distributions. All in all, we note that the application of the gradual-phase correction gives rise to more pronounced dimmings.

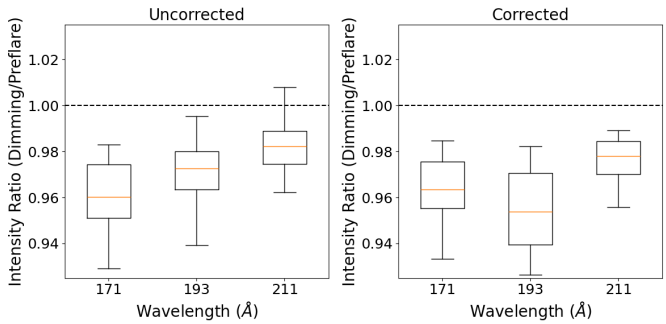

Fig. 3: Boxplots of $d_{dimming}$. The left panel has boxplots of $d_{dimming}$ from the uncorrected light curves. The right panel has boxplots $d_{dimming}$ from the corrected light curves

2.3. Construction of Sun-as-a-star DEMs

The DEMs and the respective errors were computed using the method and associated software described in (Hannah & Kontar 2012). This regularized method is widely used by the solar physics community. The DEM was computed using intensities in all six EUV channels of AIA and for the temperature range of $10^{5.0}$ K to $10^{7.5}$ K. The input intensities are the temporally averaged Sun-as-a-star intensities of each temporal window (pre-event, uncorrected dimming, corrected dimming) as defined in the previous section. For the calculation of the errors in the average intensities, we considered both shot and read noise by taking into account that the employed intensities correspond to both spatial (over the 4096×4096 pixels of each AIA image) and temporal (over the 200 images of the pre-event and dimming windows) averages.

In Fig. 4 we present the DEMs of the event in Fig. 2 for the three temporal windows in Fig. 2, i.e., pre-event, dimming uncorrected, dimming corrected. In all cases we see that in the temperature range of $\approx 10^{5.7}$–$10^{6.3}$ K the DEM corresponding to the dimming temporal window is below that of the pre-event window. In the temperature range of $\approx 10^{5.7}$–$10^{6.0}$ K the DEM corresponding to the dimming window from the corrected intensities is greater than the one corresponding to the uncorrected intensities, but their differences are smaller than the respective errors. From $10^{6.0}$ to $10^{6.3}$ K the DEM calculated by using the corrected light curves is below the DEM calculated by using the uncorrected light curves (as expected), and are mainly outside of the other's error bars, and are therefore distinguishable. The DEMs corresponding to both the corrected and uncorrected dimming windows lie below the pre-event DEM across the entire temperature range of $10^{5.7}$–$10^{6.3}$ K. However, it is only above $10^{5.8}$ K that the differences between the dimming and pre-event DEMs exceed the respective uncertainties for both the corrected and uncorrected data.

To grasp the general behavior of the dimmings in the DEM for all analyzed events, we created boxplots (Fig. 5) of the ratio ($d_{\rm DEM}^{\rm dimming}$) of the DEM during dimming to that before each event. The quantity $d_{\rm DEM}^{\rm dimming}$ is defined as $DEM^{\rm dimming}(T_*)/DEM^{\rm before}(T_*)$, where $DEM^{\rm dimming}(T_*)$ and

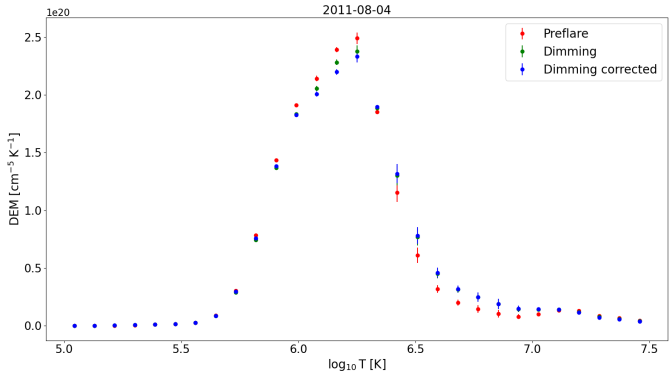

Fig. 4: DEM as a function of temperature for the event in Fig. 2. The red circles indicate the DEMs of the pre-event window, green circles indicate the DEMs of the dimming window made by using the uncorrected light curves, and the blue circles indicate the dimming window made by using the corrected light curves. The respective error bars were calculated via error propagation of the input intensities.

$DEM^{\text{before}}(T_*)$ correspond to the DEM value at a given temperature T_* during the dimming and before the start of the associated flare, i.e., corresponding to the calculations performed over the green and red shaded boxes of Fig. 2, respectively.

Figure 5 consists of two panels. The left includes $d_{\text{DEM}}^{\text{dimming}}$ calculated from the uncorrected light curves. In the right panel $d_{\text{DEM}}^{\text{dimming}}$ is calculated from the corrected light curves. We plot the results for the temperature range from $10^{5.7}$ to $10^{6.3}$ K, i.e., the range where the three AIA dimming channels (171, 193, and 211 Å) exhibit their peak temperature response.

In the left panel (uncorrected data) of Fig. 5, we see that the most pronounced dimming appears in the first half of the temperature range($\approx 10^{5.7} - 10^{6.0}$ K). For the entire temperature range of the panel, the median values of the boxplots lie in the range 0.92–0.98. The $d_{\text{DEM}}^{\text{dimming}}$ distributions have greater dispersions for the cooler temperatures, as indicated by the extents of the boxes and the whiskers. In the right panel, $d_{\text{DEM}}^{\text{dimming}}$ gets smaller in the second half of the temperature range (past $10^{6.0}$ K). For the entire temperature range of the panel, the median values of the boxplots lie in the range 0.93–0.97. In the first half of the range, the median values are slightly above those shown in the left panel, but for the second half of the range, the median values are below the respective ones in the left panel. In addition, in the first half of the temperature range, the $d_{\text{DEM}}^{\text{dimming}}$ distributions have greater dispersion than those of the second half, as indicated by the extents of the boxes and the whiskers. To summarize, we see signatures of the dimming observed in the 171, 193, and 211 Å AIA channels in the DEMs, in the temperature range that corresponds to those channels' responses. The application of the gradual correction shifts the range in which the dimming signature is more pronounced from $\approx 10^{5.7} - 10^{6.0}$ K to $\approx 10^{6.0} - 10^{6.3}$ K. This shift may indicate that plasma contributing to the gradual phase of the flare has a temperature of $\approx 10^{6.0} - 10^{6.3}$ K, which is also the temperature of the plasma that is evacuated during the eruption.

For all but two temperatures of the corrected boxplots in the right panel of Fig. 5, the upper whiskers reach or exceed 1. This is not caused by a single event in all considered temperature bins, but rather it corresponds to a different event per temperature bin.

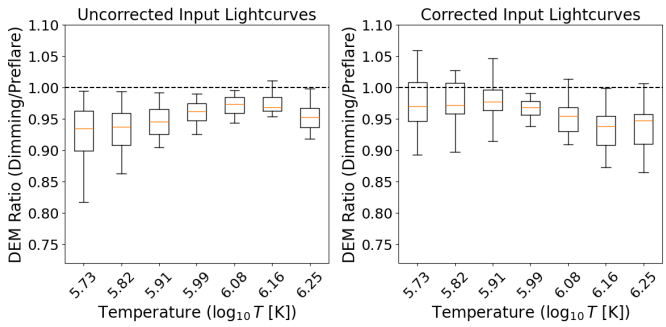

Fig. 5: Boxplots of $d_{\text{DEM}}^{\text{dimming}}$. The left panel has boxplots of $d_{\text{DEM}}^{\text{dimming}}$ calculated by the uncorrected light curves. The right panel has boxplots $d_{\text{DEM}}^{\text{dimming}}$ calculated by the corrected light curves

3. Discussion and conclusions

In this work we studied 16 major (above M1.0 of the GOES classification) eruptive flares, i.e., associated with CMEs using Sun-as-a-star observations in the six EUV channels of AIA.

Our main results are the following:

1. We detected dimmings in the light curves of the Sun-as-a-star observations at the 171, 193, and 211 Å channels. The median values of the dimmings lie around 3%. When the light curves are corrected for the gradual phase of the flare, the dimmings show a drop in their median value of a few percent (up to 5%), but they remain in the same order of magnitude.
2. We also see these dimmings in DEM calculations, in the temperature range that corresponds to the above dimming channels. The behavior of DEM is similar to that of the light curves regarding the gradual phase correction. For the $d_{\text{DEM}}^{\text{dimming}}$ calculated using the uncorrected light curves, the mark of dimming is more pronounced in the temperature range $10^{5.7} - 10^{6.0}$ K, while for the $d_{\text{DEM}}^{\text{dimming}}$ calculated using the corrected light curves the mark of the dimming is more pronounced in the temperature range of $10^{6.0} - 10^{6.3}$ K.
3. We demonstrated that the gradual-phase correction influences both the intensities and the DEMs of the dimmings.

Dissauer et al. (2018) analyzed 62 coronal dimmings associated with eruptive flares using spatially resolved AIA data studied in light curves corresponding to the respective active regions. In contrast to the present study, their dataset also includes events below the M class threshold of the GOES classification, as well as multiple CMEs that are not halo events. They found that dimming occurs primarily in the 171, 193, and 211 Å channels; the mean brightness decreases by about 60% from pre-event levels during the dimming phase. This drop, measured with spatially resolved data, is larger than that found in our spatially averaged analysis, as expected. Nonetheless, the spectral range, and therefore temperature range, over which they detect dimming is consistent with our results.

Tian et al. (2012) and Vanninathan et al. (2018) presented DEM curves for two spatially resolved coronal dimmings associated with the 2006 December 15 and 2012 March 14 eruptive flares (GOES class X1.5 and M2.8; see Fig. 16 in Tian et al. 2012 and Fig. 9 in Vanninathan et al. 2018, respectively). Tian et al. (2012) used data from the EUV Imaging Spectrometer on board Hinode, while Vanninathan et al. (2018) used data from AIA.

However, these two events are not included in our analysis. The reason for the 2006 December 15 event is that we used data from AIA, which started operating in 2010. The 2012 March 14 event was recorded by AIA, but it is deemed unacceptable for our analysis, because its Sun-as-a-star light curves for the 171, 193, and 211 Å channels have a downward trend in the pre-event window.

In both events, coronal dimmings can be seen in the corresponding DEMs in the temperature range of $\approx 10^{6.0} - 10^{6.3}$ K. The DEM peak drops approximately from $10^{21.7}$ to $10^{20.9}$ $cm^{-5}K^{-1}$ for the former event, and from approximately 2×10^{21} to 0.4×10^{21} $cm^{-5}K^{-1}$ for the latter event. The DEM peaks are for temperatures $10^{6.1}$ and $10^{6.2}$ K, respectively. This is consistent with our DEM curves of Fig. 4, for all cases; pre-event, dimming uncorrected, and dimming corrected. The decrease they find in their spatially resolved DEMs is significantly larger than that found for our Sun-as-as-star DEMs, which was expected. However, the temperature range where we observed dimmings in the DEM from the corrected light curves (see right panel of Fig.5) is practically identical to those of Vanninathan et al. (2018) and Tian et al. (2012). This lends additional support to our results, and is another confirmation of the importance of the gradual-phase correction for the appropriate analysis of coronal dimmings in Sun-as-a-star observations.

Given that our AIA narrowband and Sun-as-a-star observations 1) are affected by a lower spectral resolution compared to EVE, and 2) have no spatial resolution, we repeated the calculation of the DEMs of the fifth event in Table 1, this time using EVE and spatially resolved AIA observations, respectively. The employed event (see Table 1) is close to the median, i.e., sixth in the row, in terms of GOES-flare magnitude eruptive flare of our sample, and its source region was relatively far from the limb. In both cases, and for the resulting light curves, we followed the analysis steps as described in Section 2.2.

To calculate DEMs from EVE, we employed 10 s cadence EVE observations in a series of spectral lines of iron, which are presented in Table 2. The EVE lines we used are identical to those used in the study of the DEM of a flare presented by Mason et al. (2016). In the calculation of the EVE DEMs, we used the contribution functions of the considered spectral lines from the CHIANTI database (Dere et al. 1997; Del Zanna et al. 2021). Finally, for the correction of the gradual phase, and following Mason et al. (2016), we used the Fe XV 284 Å line. Next, to get spatially resolved DEMs from AIA observations, we used AIA intensities from 12 s cutouts in the six EUV channels of AIA which encompass the source AR of the associated eruptive flare of the fifth event in Table 1 (see, e.g., Fig. 6). For the cutout data, we included in our DEM calculation only pixels that exhibit dimming. To do so, we first created a mask that includes only the pixels undergoing dimming of an 193 Å image taken during the dimming window. In this channel the observed dimmings are more pronounced (see Fig.3). We applied this mask to every image and each channel to calculate the respective intensities corresponding to dimming. This was done in order to exclude the contribution of coronal loops energized by the flare in the $10^{5.7} - 10^{6.0}$ K range (which acts as the gradual-phase correction for the spatially averaged case).

In Fig. 7 we present $d_{\rm DEM}^{\rm dimming}$ for the fifth event in Table 1, as resulting from the Sun-as-a-star AIA observations discussed in Section 2 and the EVE and AIA cutout observations described above. From Fig. 7 we see that $d_{\rm DEM}^{\rm dimming}$, with the exception of the temperatures from 5.7–5.8 (in logT), takes similar values to the AIA Sun-as-a-star and EVE datasets. Moreover, in both cases, the dimming in the DEM, i.e., $d_{\rm DEM}^{\rm dimming}$ values below 1, can be found in the temperature range of $\approx 10^{5.8} - 10^{6.2}$ K: the minimum of $d_{\rm DEM}^{\rm dimming}$ takes values of ≈ 0.9 and 0.95, respectively. The dimming in the AIA cutout DEM behaves similarly to its respective full-disk version, and at around minimum $d_{\rm DEM}^{\rm dimming}$ is more pronounced. It is detected in the temperature range of $\approx 10^{6.0} - 10^{6.3}$ K, which is similar, but does not fully coincide with the respective range from the Sun-as-a-star AIA observations. The $d_{\rm DEM}^{\rm dimming}$ reaches values as low as ≈ 0.75. This was largely expected, given that with our spatially resolved AIA cutout observations we focused only on the AR and its surroundings from which the analyzed eruptive flare originated. In summary, the results of the DEM comparisons discussed above supply additional credibility to our employed use of Sun-as-a-star AIA observations to search for signatures of eruption-related dimmings in DEMs.

A natural next step in our analysis will be to extend our analysis to more events and supply DEM comparisons for additional events using EVE and spatially resolved AIA observations. It will also be interesting to see whether dimmings in DEM could be found in Sun-as-a-star observations of weaker eruptive flares (i.e., below the M class of the GOES classification).

Table 2: Spectral lines observed by EVE used in the calculation of the DEMs of the fifth event in Table 1.

Ion	Wavelength (Å)	Dimming line	log(T) (K)
Fe XVIII	94.0	No	6.85
Fe VIII	131.0	No	5.75
Fe IX	171.0	Yes	5.90
Fe X	177.0	Yes	6.05
Fe XI	180.0	Yes	6.10
Fe XII	195.0	Yes	6.20
Fe XIII	202.0	Yes	6.30
Fe XIV	211.0	Yes	6.30
Fe XV	284.0	No	6.35
Fe XVI	335.0	No	6.45

Notes. First column: Emitting ion; second column: Wavelength in Å ; third column: Detection of dimming; fourth column: Logarithm of the formation temperature of the spectral line.

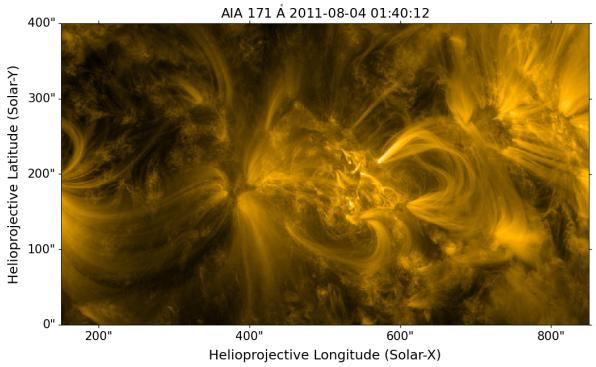

Fig. 6: Field of view of the AIA cutout images used in the spatially resolved DEM calculations of the fifth event in Table 1, shown here in a sample 171 Å channel image.

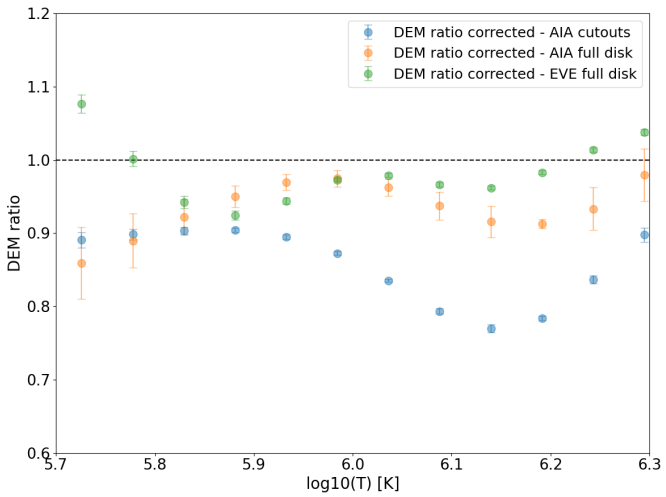

Fig. 7: $d_{\mathrm{DEM}}^{\mathrm{dimming}}$ calculated from the corrected light curves for the event 5 in Table 1. Orange filled circles: AIA Sun-as-a-star observations; green filled circles: EVE observations; blue filled circles AIA spatially resolved observations.

Our study is timely in view of the proposed mission concepts to take time-resolved EUV observations of Sun-like stars including the Normal-incidence Extreme Ultraviolet Photometer (NExtUP) Drake et al. (2021) and the Extreme-ultraviolet Stellar Characterization for Atmospheric Physics and Evolution mission (France et al. (2022)).

Data availability

The figures analogous to Fig. 1 for the remaining events in our dataset are archived and publicly available on Zenodo at `https://doi.org/10.5281/zenodo.17517487`.

Acknowledgements. The authors express their thanks to the referee, and the Editor, Maria Madjarska, for useful comments and suggestions which improved the manuscript. The authors thank Georgios Chintzoglou for useful discussions. A.M. acknowledges support by the grant of the Sectoral Development Program (ΟΠΣ 5223471) of the Ministry of Education, Religious Affairs and Sports, through the National Development Program (NDP) 2021-25. A.M. and S.P. acknowledge support by the ERC Synergy Grant 'Whole Sun' (GAN: 810218). The authors have used data from the SOHO LASCO CME Catalog. This CME catalog is generated and maintained at the CDAW Data Center by NASA and The Catholic University of America in cooperation with the Naval Research Laboratory. SOHO is a project of international cooperation between ESA and NASA. The authors also used data provided courtesy of SolarMonitor.org and data from the Solar Demon database of SIDC. The authors acknowledge the use of data from the CHIANTI atomic database. CHIANTI is a collaborative project involving George Mason University, the University of Michigan (USA), University of Cambridge (UK) and NASA Goddard Space Flight Center (USA).

References

Airapetian, V. S., Barnes, R., Cohen, O., et al. 2020, Int. J. Astrobiol., 19, 136
Aschwanden, M. J., Nitta, N. V., Wuelser, J.-P., et al. 2009, ApJ, 706, 376
Chen, P. F. 2011, Liv. Rev. Sol. Phys., 8, 1
Del Zanna, G. & Mason, H. E. 2018, Liv. Rev. Sol. Phys., 15, 5
Del Zanna, L. et al. 2021, ApJ, 909, 38
Dere, K. P. et al. 1997, A&AS, 125, 149
Dissauer, K., Veronig, A. M., Temmer, M., Podladchikova, T., & Vanninathan, K. 2018, ApJ, 863, 169
Drake, J. J., Cheimets, P., Garraffo, C., et al. 2021, in Society of Photo-Optical Instrumentation Engineers (SPIE) Conference Series, Vol. 11821, UV, X-Ray, and Gamma-Ray Space Instrumentation for Astronomy XXII, ed. O. H. Siegmund, 1182108
France, K., Fleming, B., Youngblood, A., et al. 2022, J. Astron. Telesc. Instrum. Syst., 8, 014006
Gallagher, P. T., Moon, Y. J., & Wang, H. 2002, Sol. Phys., 209, 171
Hannah, I. G. & Kontar, E. P. 2012, A&A, 539, A146
Harra, L. K. & Sterling, A. C. 2001, ApJ, 561, L215
Hernandez Camero, J., Green, L. M., & Piñel Neparidze, A. 2025, ApJ, 979, 63
Hudson, H. S., Acton, L. W., & Freeland, S. L. 1996, ApJ, 470, 629
Jain, S., Podladchikova, T., Chikunova, G., Dissauer, K., & Veronig, A. M. 2024, A&A, 683, A15
Jin, M., Cheung, M. C. M., DeRosa, M. L., Nitta, N. V., & Schrijver, C. J. 2022, ApJ, 928, 154
Kraaikamp, Emil & Verbeeck, Cis. 2015, J. Space Weather Space Clim., 5, A18
Lammer, H., Lichtenegger, H. I. M., Kulikov, Y. N., et al. 2007, Astrobiology, 7, 185
Lemen, J. R., Title, A. M., Akin, D. J., et al. 2012, Sol. Phys., 275, 17
Loyd, R. O. P., Mason, J. P., Jin, M., et al. 2022, ApJ, 936, 170
Mason, J. P., Woods, T. N., Caspi, A., Thompson, B. J., & Hock, R. A. 2014, ApJ, 789, 61
Mason, J. P., Woods, T. N., Webb, D. F., et al. 2016, ApJ, 830, 20
Mason, J. P., Youngblood, A., France, K., Veronig, A. M., & Jin, M. 2025, ApJ, 988, 167
McCauley, P. I., Su, Y. N., Schanche, N., et al. 2015, Sol. Phys., 290, 1703
Patsourakos, S., Vourlidas, A., & Kliem, B. 2010, A&A, 522, A100
Reinard, A. A. & Biesecker, D. A. 2008, ApJ, 674, 576
Robbrecht, E., Patsourakos, S., & Vourlidas, A. 2009, ApJ, 701, 283
Samara, E., Patsourakos, S., & Georgoulis, M. K. 2021, ApJ, 909, L12
Temmer, M. 2021, Liv. Rev. Sol. Phys., 18, 4
Tian, H., McIntosh, S. W., Xia, L., He, J., & Wang, X. 2012, ApJ, 748, 106
Vanninathan, K., Veronig, A. M., Dissauer, K., & Temmer, M. 2018, ApJ, 857, 62
Veronig, A. M., Dissauer, K., Kliem, B., et al. 2025, Liv. Rev. Sol. Phys., 22, 2
Veronig, A. M., Odert, P., Leitzinger, M., et al. 2021, Nat. Astron., 5, 697
Vourlidas, A., Patsourakos, S., & Savani, N. P. 2019, Phil. Trans. R. Soc. A., 377, 20180096
Webb, D. F. & Howard, T. A. 2012, Liv. Rev. Sol. Phys., 9, 3
Woods, T. N., Eparvier, F. G., Hock, R., et al. 2012, Sol. Phys., 275, 115
Xu, Y., Tian, H., Hou, Z., et al. 2022, ApJ, 931, 76
Xu, Y., Tian, H., Veronig, A. M., & Dissauer, K. 2024, ApJ, 970, 60
Yashiro, S., Gopalswamy, N., Michalek, G., et al. 2004, J. Geophys. Res. (Space Phys.), 109, A07105
Zhang, J., Temmer, M., Gopalswamy, N., et al. 2021, Prog. Earth Planet Sci., 8, 56